



Full-cycle study on developing a novel structured micromixer and evaluating the nanoparticle products as mRNA delivery carriers

Gi-Su Na^a, Jeong-Un Joo^a, Joo Young Lee^b, Yejin Yun^b, Byung Kwon Kaang^a, Joo-Sung Yang^{b,*}, Kyungjin Kim^{b,*}, Dong-Pyo Kim^{a,*}

^a Center for Intelligent Microprocess of Pharmaceutical Synthesis, Department of Chemical Engineering, Pohang University of Science and Technology (POSTECH), Pohang 37673, Republic of Korea

^b Research Center, ST Pharm, Ansan-si, Gyeonggi-do 15610, Republic of Korea



ARTICLE INFO

Keywords:
Microfluidics
Dual vortex
3D-printing
Uniform nanoparticles
mRNA delivery
Consistent production

ABSTRACT

Achieving precise control of nanoparticle size while maintaining consistency and high uniformity is of paramount importance for improving the efficacy of nanoparticle-based therapies and minimizing potential side effects. Although microfluidic technologies are widely used for reliable nanoparticle synthesis, they face challenges in meeting critical homogeneity requirements, mainly due to imperfect mixing efficiency. Furthermore, channel clogging during continuous operation presents a significant obstacle in terms of quality control, as it progressively impedes the mixing behavior necessary for consistent nanoparticle production for therapeutic delivery and complicates the scaling-up process. This study entailed the development of a 3D-printed novel micromixer embedded with hemispherical baffle microstructures, a dual vortex mixer (DVM), which integrates Dean vortices to generate two symmetrical counter-rotating intensified secondary flows. The DVM with a relatively large mixer volume showed rapid mixing characteristics even at a flow rate of several mL min^{-1} and produced highly uniform lipids, liposomes, and polymer nanoparticles in a size range (50–130 nm) and polydispersity index (PDI) values below 0.15. For the evaluation of products, SARS-CoV-2 Spike mRNA-loaded lipid nanoparticles were examined to verify protein expression in vitro and in vivo using firefly luciferase (Fluc) mRNA. This showed that the performance of the system is comparable to that of a commercial toroidal mixer. Moreover, the vigorous in-situ dispersion of nanoparticles by harnessing the power of vortex physically minimizes the occurrence of aggregation, ensuring consistent production performance without internal clogging of a half-day operation and facilitating quality control of the nanoparticles at desired scales.

1. Introduction

Nanotechnology has attracted considerable attention in the field of drug delivery owing to its advantages such as specific cell targeting, enhanced permeation and retention (EPR) effect, and reduced cytotoxicity, overcoming the limitations of conventional delivery methods by handling biological barriers in organs [1–3]. To maximize consistent therapeutic efficacy with minimal side effects, precise control of their size is critical, as deviations from the target size can lead to toxicity due to accumulation in undesired organs or cells depending on the specific disease and target organ [4–6]. In pursuit of these objectives, the application of microfluidics has emerged as an indispensable approach that meets complex requirements and new demands owing to its high mass transfer and precise process control [7,8].

However, continuous nanoparticle production via a microfluidic mixer poses challenges for solution mixing and has implications for the aggregation and consistency of physicochemical properties [9,10]. Due to material vulnerabilities and structural limitations, the micromixers proposed thus far face challenges in maintaining consistent mixing performance or the use of either high anti-solvent to good-solvent ratios (>10), or high industrial flow rates over $\sim 10^1 \text{ mL min}^{-1}$. In addition, gradual channel deformation and clogging due to the surface adhesion of the precursors make it infeasible to produce uniformly over a long period of time [11–13]. As for the manufacturing technology of the micromixer, conventional photolithography or injection molding techniques suffer from the narrow availability of suitable resins, most of which have low solvent resistance. These subtractive manufacturing processes make it difficult to implement complex and three-dimensional

* Corresponding authors.

E-mail addresses: joosung.yang@stpharm.co.kr (J.-S. Yang), kyungjin.kim@stpharm.co.kr (K. Kim), dpkim@postech.ac.kr (D.-P. Kim).

structural concepts [14,15]. On the other hand, 3D-printing is a promising alternative as the additive manufacturing process is easy to construct the desired monolithic structures using sophisticated design concepts. However, it is still not easy to manufacture a small volumetric mixer with high resolution; therefore, bulky channels with large dimensions are generally fabricated. In this case, expensive precursor reagents are inevitably consumed when a high mixing efficiency is feasible only under high flow rates [16–18].

It is well known that baffle structures inside the mixer induce secondary flows and improve mixing efficiency [19–21]. However, the widely used 2D baffle is prone to cause nanoparticles to adhere to the corner as a structural dead volume, which gradually degrades the performance of the mixer, including the inner flow pressure, along with usage time [11,22]. Accordingly, nanoparticle properties may be uneven in terms of time dependence. Therefore, it is necessary to develop a new concept for a micromixer that enables ultrafast mixing at low flow rates and facilitates the control of the desired production scale without channel clogging, even during long-term operation. In addition, to use the newly developed mixer in practice, it is essential to thoroughly verify the preliminary performance of the produced functional nanoparticles.

Recently, mRNA-loaded lipid nanoparticles (mRNA-LNPs) as a Covid-19 vaccine have significantly contributed to the promotion of human health during the pandemic [23,24]. Gene therapy has emerged as an innovative approach for the prevention and treatment of various diseases [25–27]. In these cases, it should not be overlooked that accurate investigation of protein expression enables various applications, in addition to excellent intracellular delivery efficiency and low immunogenicity. The developed mixers demonstrate an early stage of particle manufacturing capability [10,18,28,29]. Few studies have investigated the efficacy of nanoparticles produced *in vivo* and *in vitro* in comparison to those produced using one of commercial micromixers, the toroidal mixer (NanoAssemblr Ignite). Thus, beyond the evaluation of physical properties after synthesizing nanoparticles using a mixer, it is essential to accurately confirm the *in vitro* and *in vivo* efficacy to understand the pharmacological profile.

Herein, we present a new conceptual micromixer embedded with 3D hemispherical baffle structures, called a dual vortex mixer (DVM), which was designed using a thorough computational fluid dynamics (CFD) simulation and then fabricated using a 3D-printer (**Scheme 1**). The DVM, with a length of only 3.9 mm of 3 baffles, enables ultrafast mixing within a few milliseconds at total flow rates of several mL min^{-1} with low anti-solvent ratio by inducing two symmetric vortices of extensive intensity (**Fig. 1D** and **Fig. S1**), thereby bridging the

operational gap between microfluidic mixers. Highly uniform polymeric nanoparticles, liposomes, and mRNA-LNPs with sizes below 100 nm and a PDI value below 0.1 were produced across a wide range of concentrations and throughput. With respect to mRNA-LNPs, the DVM demonstrated an equivalent performance to a commercial toroidal mixer by fully investigating the protein expression *in vitro* through SARS-CoV-2 Spike mRNA as well as *in vivo* tests using FLuc mRNA. Interestingly, minimal dead volume in the DVM platform with the round corners of the hemispherical baffles, and the strong swirling effect provides vigorous dispersion of the as-synthesized nanoparticles, retaining uniform production of particles even during 12 h of nonstop operation. Experimentally, the clogging is approximately 179 times lower than that of a commercial toroidal mixer. Based on the full-cycle study, this new platform potentially serves as a versatile tool for nano-carrier production, both at laboratory scale and in parallelized scaled-up systems for industrial production.

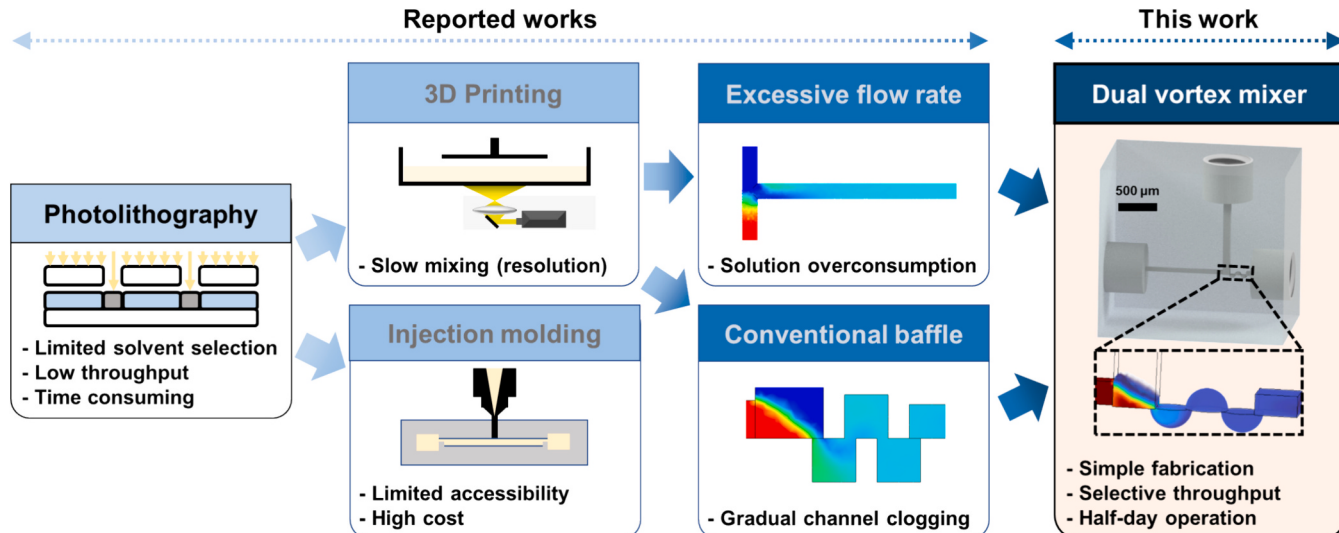
2. Materials and methods

2.1. Materials

Ethyl alcohol (EtOH), tetrahydrofuran (THF), acetone, sodium chloride, sodium acetate solution, acetonitrile (ACN), Polycaprolactone (PCL), 1,1,2,2-Tetraphenylethylene (TPE), cholesterol (Chol), and Triton X-100 were purchased from Sigma-Aldrich. 1-Palmitoyl-2-oleoyl-sn-glycero-3-phosphocholine (POPC), 1,2-distearoyl-sn-glycero-3-phosphocholine (DSPC), 1,2-Dimyristoyl-rac-glycero-3-methoxypolyethylene glycol-2000 (DMG-PEG 2000) were purchased from Avanti Polar Lipids, Inc. (heptadecan-9-yl 8-((2-hydroxyethyl)(6-oxO-6-(undecyloxy) hexyl) amino) octanoate) (SM-102) was purchased from Xiamen Sinopeg Biotech Co. Ltd. Poly(ethylene glycol) methyl ether-*block*-poly(lactide-co-glycolide) (PEG_{5k}-PLGA_{55k}) was purchased from Creative PEGWorks. SARS-CoV-2 Spike mRNA and firefly luciferase mRNA (FLuc mRNA) were obtained from ST Pharm Co. Ltd. (Korea).

2.2. 3D-printed fabrication of the micromixers

The 3D-printed micromixers were designed using a computer-aided design (CAD) software (Autodesk Inventor). In order to facilitate stable injection of two different solutions, a 5 mm thread (1/4–28 Flat-Bottom for 1/16") was introduced at the injection site, following intervals longer than the theoretical flow stabilization length of 10 mm. This modification allowed for a seamless connection to the XP-235



Scheme 1. Evolution of micromixers (reported works) and dual vortex mixer (DVM) for overcoming their limitations.

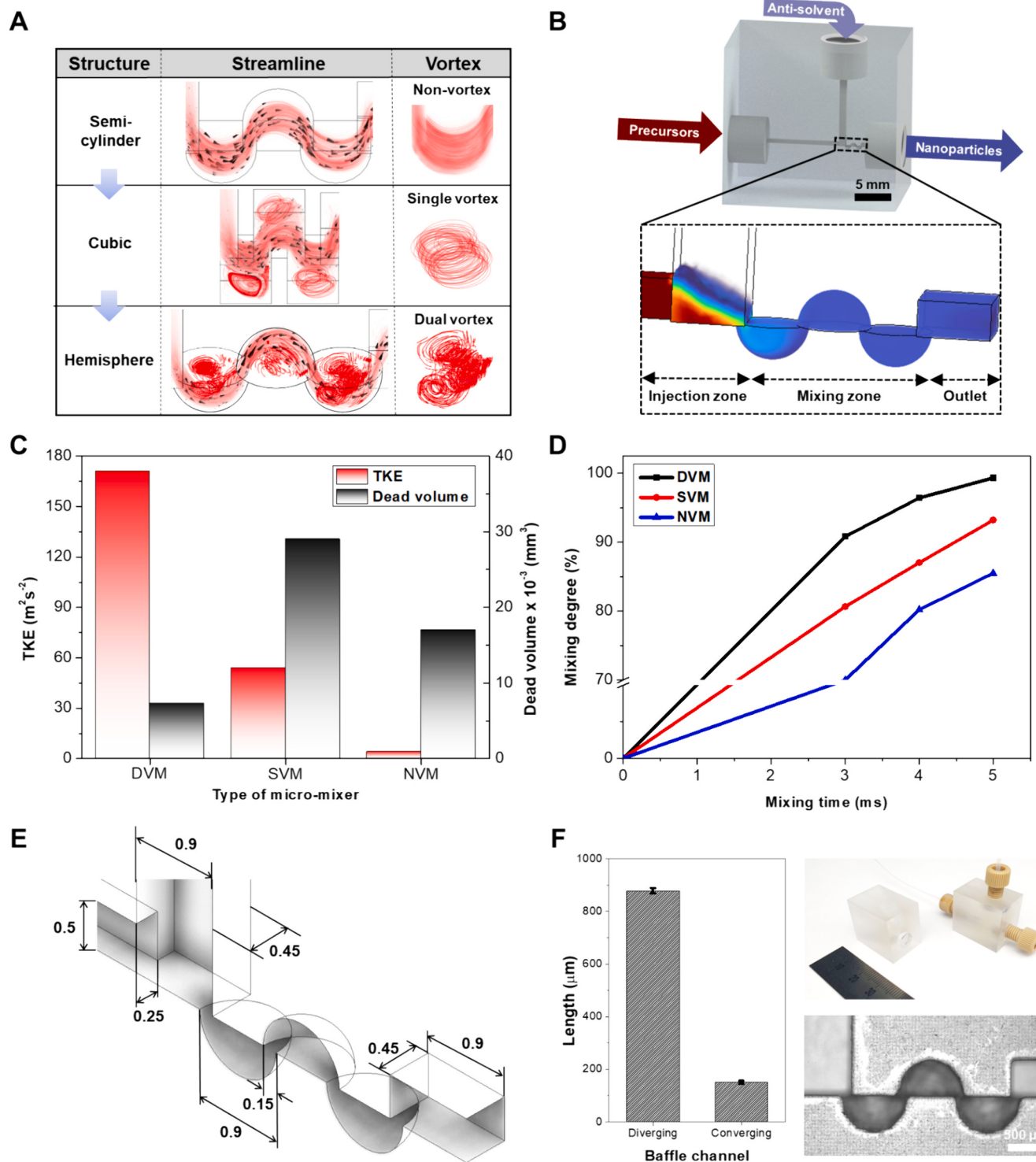


Fig. 1. Design and CFD-based optimization of a dual vortex mixer (DVM) for continuous production of polymer- and lipid-based nanoparticles. (A) Schematic representation showing changes in the vortex formation within the channel as a result of variations in the baffle structure. (B) A comprehensive diagram and detailed components of the DVM. To prevent leakage during the liquid injection process, there are two inlet and outlet sections designed to allow for fitting connections. (C) Comparison of TKE and dead volume size between SVM and NVM devices with the same specifications as the optimized DVM device. (D) At a flow rate of 9 mL min⁻¹, the DVM device achieves perfect ultrafast mixing within 5 ms, with over 99% efficiency. (E) Cross-sectional details of optimized virtual DVM and (F) Visual images and detailed dimensions of 3D-printed DVM.

fitting (IDEX Health & Science), and the CAD file was printed using a DLP-based 3D-printer (Pico 2 HD, Asiga) using a poly(methyl methacrylate) (PMMA)-based commercial resin (PlasCLEAR) which has a chemical resistance against various organic solvents such as acetone and ethanol. Each layer was printed in 25 μm and laminated by photocuring.

To remove the uncured residual resin inside the printed device, isopropanol (IPA) was used, and air was flushed through the mixer to further remove the IPA. This process was repeated until no resin was visible at either the inlet or outlet. Finally, the rinsed device was post-cured in a UV chamber (Asiga Flash), which transformed the resin

into a fully polymerized object. For the two-piece assembly type of micromixer, the monolithic device as aforementioned was divided into two halves, and each part was designed separately. After printing, the two components were placed on a stainless-steel metal frame secured with screws.

2.3. Computational fluid dynamics (CFD) simulation of micromixers

Numerical CFD studies were conducted to evaluate the degree of mixing, TKE, and dead volume inside the baffles. Fluid flow within a micromixer can be described by the Navier–Stokes equation, species-transport equation, and the mass-conversion equation. To select the appropriate viscous model, the maximum Reynolds number was calculated for the baffle section between the structures with the smallest areas on each virtual device. The density and viscosity of the water-ethanol mixture based on the total flow rate and the flow rate ratio were calculated as follows:

$$\rho_{\text{mixture}} = \frac{\sum_i v_i \rho_i}{\sum_i v_i} \quad \mu_{\text{mixture}} = \sum_i x_i \mu_i$$

where ρ_{mixture} and μ_{mixture} are the density and viscosity of the water-ethanol mixture, and v_i , ρ_i and x_i represent the volume fraction, density and mole fraction of component i , respectively. The hydraulic diameter in the baffle section were calculated as follows:

$$d_h = \frac{4A}{d}$$

where d_h is hydraulic diameter of baffle, and A and d are the cross-sectional area, and perimeter of the baffle.

As the Reynolds numbers are varied from laminar to transition region depends on the total flow rate, shear-stress transport (SST) $k-\omega$ standard turbulence model which merged $k-\epsilon$ turbulence and $k-\omega$ turbulence models was used for calculation [30,31]. Assuming a steady state, the governing equation for fluid flow can be simplified as follows:

$$\rho v \bullet \nabla v = -\nabla p + \mu \nabla^2 v + \rho g: \text{Navier–Stokes equation}$$

$$\nabla \bullet v = 0: \text{Mass-conversion equation}$$

$$\nabla \bullet (\rho v Y_i) = -\rho D_i \nabla Y_i: \text{Species-transport equation}$$

where ρ is the fluid density, v is the fluid linear velocity, p is the pressure, μ is the fluid dynamic viscosity, g is the gravitational acceleration, and Y_i is the mass fraction of each species i . Molecular diffusivity of $1.23 \times 10^{-9} \text{ m}^2 \text{ s}^{-1}$ was used for D_i . The governing equations were solved with appropriate boundary conditions (no-slip boundary conditions on the channel walls, mass flow rate for the inlets, outflow conditions for the outlets, and zero normal gradients for all flow variables except pressure). The equations were discretized based on the finite volume method, and the commercial numerical software FLUENT 2022 R2 (ANSYS, Inc.) was used for numerical simulation. The density and viscosity of ethyl alcohol (790 kg m^{-3} , $0.0012 \text{ kg m}^{-1} \text{ s}^{-1}$) and water (998.2 kg m^{-3} , $0.001003 \text{ kg m}^{-1} \text{ s}^{-1}$) were used for fluid properties. The portion of the computational domain which the velocity magnitude fell below 5% of the maximum velocity at a given time was labelled as dead volume [32,33]. To quantify the TKE depending on the baffle geometry, the sum of the value corresponding to each node from volume rendering was calculated as the TKE cannot be directly obtained from FLUENT. The mixing degree depending on the time was calculated by the following mixing efficiency.

$$\eta = 1 - \sqrt{\sigma^2 / \sigma_{\max}^2}, \text{ where } \sigma = \sqrt{\frac{1}{N} \sum_{j=1}^N (c_j - c_{in})^2}$$

The standard deviation of concentration across the cross-section, considers N , the number of nodes within the cross-section. c_j represents the local concentration at the j -th node within the cross-section, whereas c_{in} is the average concentration at the inlet. Additionally, σ_{\max} signifies the maximum standard deviation of the concentration observed [19].

2.4. Preparation of PCL nanoparticles

PCL (average M_w approximately 14,000, average M_n approximately 10,000) was dissolved in dimethylformamide (DMF) and deionized water was used for precipitation of PCL nanoparticles [34]. The PCL precursor solution and deionized water were injected using two 20 mL syringes (Air-Tite Products, Inc.). Each syringe was attached to a distinct syringe pump (PHD Ultra, Harvard Apparatus), and flow rate ratio (FRR), which is the volumetric flow rate of the antisolvent divided by the volumetric flow rate of the carrier solution, ranging from 3 to 9 was used to control the flow rate of each pump. The syringe for injection of antisolvent was connected vertically, whereas the syringe for injecting the polymer was connected parallel to the outlet.

2.5. Preparation of PEG-PLGA nanoparticles

PEG_{5k}-PLGA_{55k} was dissolved in acetonitrile (ACN) and deionized water was used as an antisolvent for precipitation of the PEG-PLGA nanoparticles using the injection method as aforementioned.

2.6. Preparation of POPC liposomes

POPC liposomes were prepared by mixing aqueous and lipid solutions. POPC and cholesterol were dissolved in ethanol at a total concentration of 10 mg mL^{-1} and a molar ratio of 55:45 [35]. The lipid solution and an aqueous buffer (saline, 154 mM NaCl) were injected into the lipid and antisolvent inlets, respectively. Self-assembled POPC liposomes were collected from the outlet stream resulting from the mixing of two adjacent streams and dialyzed overnight using dialysis sacks (MWCO 12,000 Da, Sigma-Aldrich) against 1000 times the buffer (10 mM PBS, pH 7.4) to remove the residual ethanol.

2.7. Preparation of mRNA-LNPs

Each mRNA-LNP sample was prepared to achieve a final mRNA concentration of 0.10 mg mL^{-1} , with an ionizable lipid / mRNA mass ratio of 11.5 after formulation. Briefly, a lipid solution with a total concentration of 20 mg mL^{-1} was prepared by dissolving SM-102/DSPC/Chol/DMG-PEG 2000 in ethanol at a ratio of 50/10/38.5/1.5 [36]. A sodium acetate solution with a concentration of 3 M was diluted with nuclease-free water (NFW) to a concentration of 25 mM. The pH of the sodium acetate buffer was adjusted to 5.5 using a 100 mM acetic acid solution. Prior to injection, the lipid solution and sodium acetate buffer were passed through a $0.22 \mu\text{m}$ syringe filter. The FLuc mRNA was dissolved in sodium acetate buffer. After formulation, the mRNA-LNPs were purified using the same upper method used for liposome.

2.8. Measurement of particle size and encapsulation efficiency

DLS analysis was performed using a Zetasizer Nano ZS instrument (Malvern Instruments, Ltd.) to determine the size distribution of the synthesized nanoparticles based on their intensity. For the mRNA-LNPs, the Quant-it™ Ribogreen assay (Thermo Fisher Scientific) was used to characterize the EE of mRNA. Briefly, LNPs were first diluted by using Tris-EDTA (TE) buffer until the concentration was in the range from 4 to $7 \text{ ng } \mu\text{L}^{-1}$. The diluted LNPs were treated with either TE buffer to maintain the LNP structure or 1% v/v Triton X-100 to disrupt the structure and release mRNA and then reacted with equal volume of Ribogreen solution at a 100-fold dilution. Free and total mRNA in the formulation were determined using a microplate reader (Hidex Sense, Hidex Oy) at 500 nm excitation and 520 nm emission.

2.9. Calculating the volume of micro-structure mixing inside a toroidal mixer

The volume of the toroidal mixer's (NanoAssemblr Ignite, Precision

NanoSystems) internal structure was determined by retroactively estimating the residence time with respect to water flow. In summary, the outlet of the toroidal mixer cartridge was connected to 1/16" PTFE tubing, and this tubing was connected to a syringe through a 19G needle, which was subsequently attached to a syringe pump. The syringe pump was operated at a rate of 0.05 $\mu\text{L min}^{-1}$, and the residence time was calculated by visually confirming the point at which the first structure began to fill with the fluid until the last structure was completely filled. The final volume of the toroidal mixer's internal structure was computed as an average of three independent measurements.

2.10. Comparative formulation and concentration of DVM-LNPs and toroidal-LNPs

For the formulation of DVM-LNPs and Toroidal-LNPs, a lipid solution (3.2 mg mL^{-1}) and mRNA solution were mixed at the same component and mass ratios, as aforementioned. A flow rate of 3 mL min^{-1} for the lipid solution and 9 mL min^{-1} for the buffer solution, commonly used for the operation of commercial toroidal mixers (Ignite, Ignite Dilution), was employed for both devices. When PBS dilution was performed immediately after formulation, LNPs were diluted at a 1:1 or 1:2 ratio with PBS using a T-mixer in the case of the DVM, or an Ignite Dilution cartridge with 3 inlets was used. To achieve a complete buffer environment, a centrifugal filter device (Amicon® Ultra-15, Merck Millipore) was used for diafiltration. Briefly, the purified samples were placed inside the unit, the remaining space was filled with buffer, and centrifugation was repeated at 3500 rpm for 40 min until the pH of the solution outside the membrane reached 7.4. For in vitro use, LNP loaded with SARS-CoV-2 Spike mRNA was diluted to achieve a concentration of 0.08 mg mL^{-1} of mRNA. For in vivo applications, LNP loaded with FLuc mRNA underwent the same purification process, and the final concentration of the mRNA was set at 0.10 mg mL^{-1} .

2.11. In vitro spike mRNA protein expression

HEK 293 T cells (ATCC, American Type Culture Collection) were cultured at a density of 1×10^6 cells/well for Western blot analysis. Samples containing SARS-CoV-2 Spike mRNA, including DVM-LNPs and Toroidal-LNPs, were dispersed in Opti-MEM (Reduced-Serum Medium, Gibco™) and treated with 3 μg of mRNA-LNP complex per well. Spike protein expression was measured after 24 h of incubation. Following transfection, each well was treated with sterile PBS and 200 μL of lysate complex (Cell Lysis Buffer, Invitrogen™), followed by incubation at room temperature for 10 min. Samples were then centrifuged at 13,000 rpm for 10 min before collection for analysis.

2.12. Western blot

Cell extracts were separated by 4–15% gradient SDS-PAGE (4–15% Mini-PROTEAN TGX™ Precast Protein Gels, Bio-Rad). The cell lysate proteins were transferred from the gel to a $0.2 \mu\text{m}$ PVDF membrane (Mini-format, Bio-Rad) and immunoblotted with Recombinant 2019-nCoV Spike antibody (SARS-CoV-2 Spike RBD Polyclonal Antibody, Elabscience) and GAPDH antibody (sc-47,724, Santa cruz Biotechnology). Analysis was performed using a Western blot imaging system (ChemiDoc MP Imaging System, Bio-Rad) with Western ECL solution (Clarity™ Western ECL Substrate, Bio-Rad).

2.13. In vivo luciferase protein expression

Male BALB/c mice weighing between 22 and 25 g were randomly divided into seven groups ($n = 3$ per group). These groups included a negative control group treated with PBS, three groups treated with FLuc mRNA-containing DVM-LNPs, and three groups treated with Toroidal-LNPs. Each group was administered a volume of 50 μL (containing 5 μg of mRNA) into the right quadriceps muscle of the mice. Body weight

and bioluminescence of each mouse were measured at seven time points: pre-administration and 0.5, 6, 24, 48, 72, and 6 days post-administration. Prior to image acquisition, each mouse received 100 μL of luciferin (D-Luciferin, GoldBio) at a concentration of 15 mg mL^{-1} into the abdominal cavity on both sides, followed by imaging using an IVIS Spectrum (PerkinElmer, USA) at the specified time points. After acquiring images over a period of six days, a region of interest (ROI) was defined around the injection site, and the total flux value was calculated.

2.14. Long-term operational test of the micromixers

Three assembly types of NVM, SVM, and DVM in addition to a transparent toroidal mixer were used for long-term production of nanoparticles. The TPE, with a concentration of 1 mg mL^{-1} , was dissolved in acetone. Deionized water was used as the antisolvent for continuous nanoparticle production. To prevent solvent evaporation, the beaker was sealed with parafilm and foil. An HPLC pump (PR-Class, Teledyne SSI) was connected to a beaker of deionized water to allow injection at a high flow rate. Another HPLC pump (LC-10 CE; Shimadzu) was connected to the TPE solution. To connect to the toroidal mixer, the outlets of the HPLC pumps were linked to 1/4" PTFE tubing using 316 stainless steel reducers (SS-400-6-1BT, Swagelok). The end of each tube was further connected to a 3 mm Stainless Needle Luer-lock tubing connector (KT503s, Needle store) to fit into the inlet of the toroidal mixer. The HPLC pumps were set to operate with a TPE solution flow rate of 0.9 mL min^{-1} and a deionized water flow rate of 8.1 mL min^{-1} . The pressure of the HPLC pump was continuously monitored in real time during operation to calculate the pressure difference. The resulting nanoparticles from the outlet were collected in different vials for further DLS analysis.

2.15. Visualization and quantification of channel clogging

After the completion of continuous operation (166 min for SVM, 120 min for NVM, 100 min for toroidal mixer, 166 min, and 12 h for DVMs) as aforementioned, a flow of deionized water was injected through inlet at 0.1 mL min^{-1} for 1 min to flush out any remaining solutions without affecting the clogged nanoparticle. Subsequently, the micromixers were dried in an 80°C oven for 30 min to remove any residual water inside. The remaining particles inside were then visualized and quantified for the toroidal mixer. In the case of the 3D-printed micromixers, they were disassembled before visualization and quantification. For visualization, the toroidal mixer and the disassembled micromixers were placed under a fixed UV lamp (365 nm, approximately 100 mW cm^{-2}) in a darkened state and observed under a microscope. As the intensity of the luminescence was not able to quantify directly, the clogged nanoparticles were dissolved using acetone and collected in vials for quantification. The quantity of nanoparticles was determined using a calibration curve using TPE in acetone with a wavelength of 330 nm.

3. Results and discussion

3.1. Design and optimization of DVM

We focused on three important aspects in the development of a new micromixer that can maintain ultrafast mixing performance over an extended period of time. First, the internal baffle structure within the channel induces secondary flows, which can be regulated by adjusting the flow intensity in the incidental flow direction [21,37]. Second, the use of a round-structured channel with minimal dead volume, as opposed to an angled structured channel, improves the mixing efficiency [38] and facilitates long-term continuous operation [11,39,40]. Finally, the vortex generated inside the reactor further accelerates the mixing and the dispersion of nanoparticles, preventing adhesion and agglomeration [41–43].

For a 2D baffle with a constant channel height, secondary flow-

induced vortices were formed based on subtle changes in the flow intensity. Semi-cylinder baffles did not induce a clear alteration in the direction of the fluid flow, thereby suppressing vortex formation [40]. In contrast, cubic baffles, owing to their angular structure, induced an additional flow perpendicular to the dominant flow axis, resulting in the formation of a single vortex [21]. In this context, the fundamental concept of the new micromixer entails arranging baffle structures of 3D hemispheres, consequently bestowing slightly altered micro-curvature radii upon each fluid element during the three-dimensional flow expansion. Through this approach, coherent flows and Dean vortices are induced by the divergent and convergent discharge of fluid through narrow apertures, resulting in a diagonally symmetrical dual vortex relative to the primary flow. (Fig. 1A).

To conduct a comprehensive numerical comparison of the mixer structures based on CFD simulations [44], we designed three virtual channel models, each including the injection zone and the outlet, and all having the same volume and converging channel length (Fig. 1B). These models consisted of a non-vortex mixer (NVM) with semi-cylinder baffles, a single vortex mixer (SVM) with cubic baffles, and a DVM with hemisphere baffles. Ethanol and water were selected to simulate the mixing of two solutions used in lipid nanoparticle [15,18,28,45]. We evaluated these micromixers based on their turbulent kinetic energy (TKE), which is an indicator of vortex intensity [46], formation of dead volume within the baffles, and mixing efficiency over time. In general, DVM showed remarkably enhanced secondary flow compared to SVM and NVM. By implementing a strong TKE, minimizing dead volume, and achieving the highest mixing efficiency, the hemispherical baffle structure outperformed the other baffle structures (Table S1, and Fig. S1). To optimize the DVM, we performed additional simulations with different baffle dimensions while maintaining a constant flow rate. A smaller converging channel improved the mixing performance owing to a stronger fluid expansion without altering the residence time per structure. The diverging channel not only influenced the expansion but also impacted the residence time per structure. Increasing the length of the diverging channel while keeping the converging channel constant results in a substantial increase in the time spent by each structure within a single baffle [47]. Consequently, this led to a lower number of structures passing through in the same timeframe, indicating a diminished mixing efficiency. Conversely, with substantially decreased diverging channels, the potential for utilizing the Dean vortex through 3D expansion flow was limited [48]. Therefore, a diameter of 900 μm was ultimately selected, maximizing the combination of residence time for the overall mixer volume and each structure individually (Table S2). The optimized DVM achieved a TKE of $171 \text{ m}^2 \text{ s}^{-2}$, exceeding the values of SVM and NVM by >3.2-fold and 41-fold, respectively, while also having a dead volume of $7.32 \times 10^{-3} \text{ mm}^{-3}$, which was less than half the size of the other models (Fig. 1C). Through these turbulent effects, DVM exhibited significantly superior mixing performance compared to SVM and NVM, achieving a mixing degree of 99.3% in just 5 ms, surpassing the respective efficiencies of 93.2% and 85.5% (Fig. 1D). The detailed dimensions of the selected DVM device are shown in Fig. 1E. Eventually, the flow rates forming symmetrical dual vortex were determined at different flow rate ratios (FRR = 3, 6, and 9). An ethanol flow rate $\geq 0.9 \text{ mL min}^{-1}$ at an FRR of 3 exhibited a distinct dual vortex that intensified at higher FRRs and was used for experimental nanoparticle production (Tables S3 to S5). The significantly lower specified flow conditions, compared to those used in general large-scale mixers produced using fabrication techniques such as 3D-printing [16,18,49], effectively mitigate excessive solution consumption during the nanoparticle optimization process.

3.2. 3D-printing of DVM and validation for chemical stability

3D-printing not only enables the facile fabrication of three-dimensional structures but also the selective use of resins to achieve high chemical stability in organic solvents used for manufacturing

nanoparticles after curing [50,51]. Digital light processing (DLP) printing is widely known for its high resolution and is therefore commonly used for the fabrication of microfluidic channels smaller than 1 mm. We selected a PMMA-based resin that exhibits negligible swelling behavior against several organic solvents including ethanol and acetone [52], which is commonly applied in the production of nanoparticles for mRNA delivery, and prevents device deformation under high-pressure conditions. Using the selected resin, we were able to promptly fabricate the entire structure of the DVM (45 min per device), including two vertical sides of a 15 mm injection zone with microstructures and a 5 mm outlet [53]. Accurate dimension of the device was verified by printing the channel cross-section exposed in half, and the lengths of the diverging and converging channels were measured through a microscope, revealing average lengths of 880 μm and 150 μm, respectively (Fig. 1F). We further confirmed that the device fabricated with this resin exhibited no leaching for even 12 h of long-term ethanol or DMF injection, as determined by gas chromatography (GC) analysis (Fig. S2). Therefore, the device possesses the requisite mechanical and chemical properties for the continuous production of particles over an extended period of time.

3.3. Production of nanoparticles for drug delivery

DVM is a versatile platform for the production of lipid- and polymer-based nanoparticles for drug delivery with high uniformity and controllable sizes. To demonstrate the capabilities of this platform, we synthesized four distinct types of nanoparticles utilizing FDA-approved materials, including polycaprolactone (PCL), and poly(ethylene glycol)-b-poly(lactide-co-glycolide) (PEG-PLGA) nanoparticles, 1-palmitoyl-2-oleoyl-sn-glycero-3-phosphocholine (POPC) liposomes, and mRNA-LNPs [23,54]. In general, upon diffusion mixing, it is often challenging to systematically control high concentration of precursors, which can lead to the formation of bimodal peaks and a broadening of the size distribution. To illustrate control over a broad concentration range of precursors and process parameters for versatile nanoparticle synthesis, each organic phase was prepared under three different concentration conditions, and the process parameters including the total flow rate (TFR) and FRR was screened. Especially, PEG-PLGA was set up to 50 mg mL^{-1} as a higher concentration than the reported [10,55]. By dynamic light scattering (DLS) analysis, highly reproducible nanoparticles were generated at both cases with diameters ranging from 50 to 130 nm and PDI of <0.15 (Fig. 2A to F). Furthermore, the size of each nanoparticle tends to decrease as the FRR and TFR increase, and as the concentration of the precursor solution decreases. These results indicate that the relatively large-volume DVM with a submillimeter diameter enables ultrafast mixing within the channel and demonstrates the ability to systematically control high concentrations of precursors without the formation of aggregated particles.

The figure of merit (Q) values as the inverse of the product of liposome diameter (d) and PDI, i.e., $Q = d^{-1} \text{ PDI}^{-1}$, are used to evaluate the performance of the micromixer devices [18]. The DVM showed exceptionally high Q values ranging from 0.08 to 0.45 for POPC liposomes, and substantially exceeded 0.15 for other nanoparticles at considerably low FRR <10 , (Fig. 2G to I). Notably, the reported works attained high Q values of 0.4 at a much higher FRR condition upto 100 [18]. Under low FRR conditions, the amount of antisolvent that needs to be removed is reduced, thereby potentially simplifying and shortening the purification process after nanoparticle production to facilitate exchange into an optimal buffer environment for subsequent storage or evaluation [56]. Next, upon generation of drug-loaded nanoparticles, it is necessary to verify high encapsulation efficiency (EE) through efficient interactions between the carrier and the therapeutic agent [8]. Accordingly, we loaded FLuc mRNA into LNPs to measure their physicochemical properties. >90% of FLuc mRNA was successfully encapsulated in each sample while maintaining high uniformity, indicating that sufficient electrostatic attraction was generated between ionizable lipids and

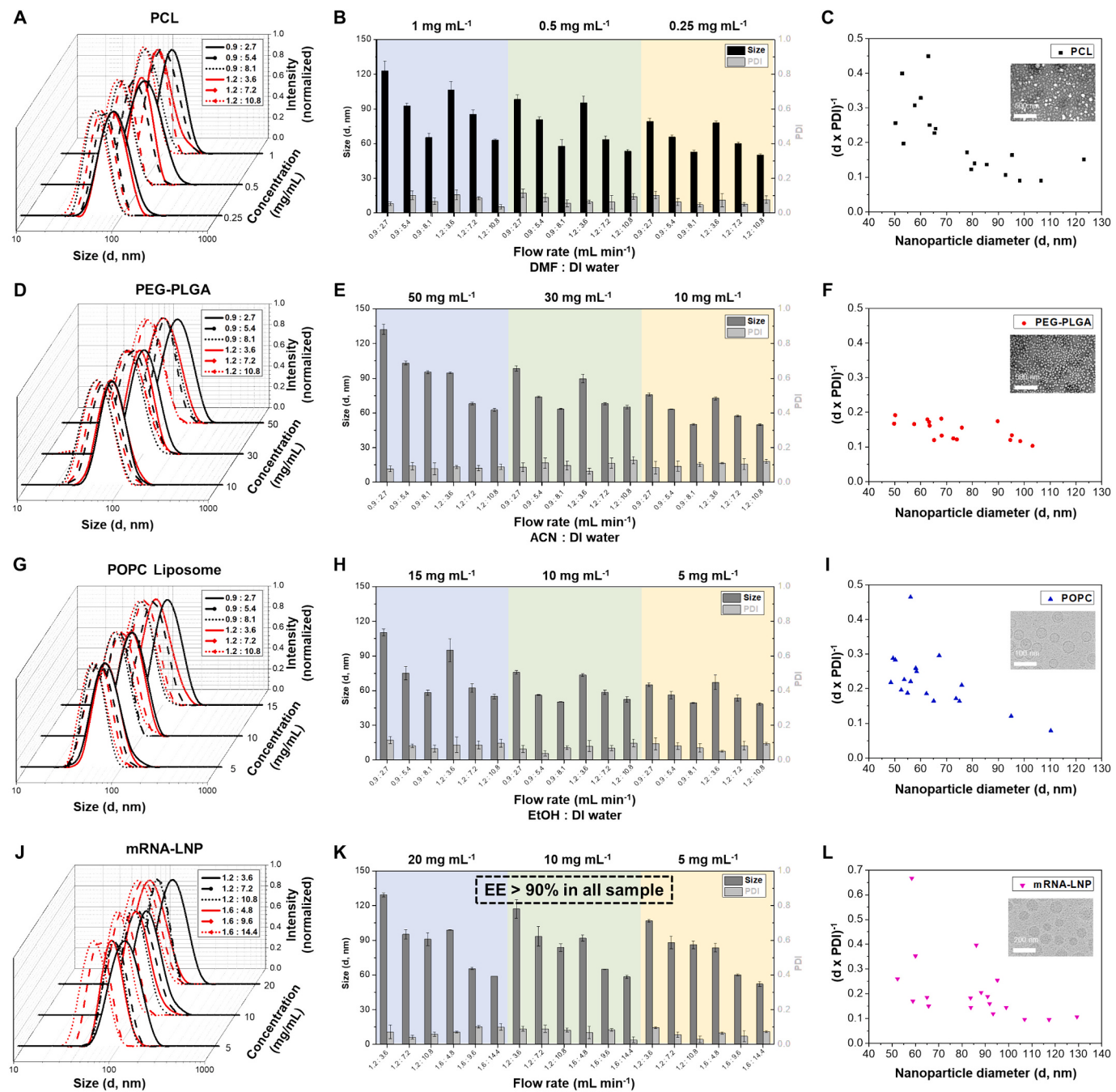


Fig. 2. Validation of DVM performance through the production of versatile nanoparticles. Normalized size distributions (left), numerical size and PDI (middle), and Q values (right) of (A to C) PCL nanoparticles, (D to F) PEG-PLGA nanoparticles, (G to I) POPC liposomes, and (J to L) mRNA-LNPs. Each distribution was averaged from independent experiments ($n = 3$). The table inside of graph depicts the ratio between the organic phase flow rate and the antisolvent flow rate (unit: mL min^{-1}).

mRNA (Fig. 2J to L and Fig. S3). The throughput of the DVM can vary depending on the type and concentration of the precursors used, as well as the desired nanoparticle size. Our results show that the production rate of DVM based on these nanoparticles can be selectively adjusted over a wide range from 54 mg h^{-1} to a maximum of 3600 mg h^{-1} .

3.4. In vitro/in vivo mRNA-LNP protein expression

To affirm performance of the DVM device in a full-cycle manner, it is essential to compare not only their characteristics of produced nanoparticles but also the biokinetic profiles with those of nanoparticles generated via commercial mixer under identical conditions. The choice

of mRNA-LNPs for this comparative study was deliberate, as it represents one of the most effective methods available for determining the efficacy of nanoparticles. As a comparison group for validation, we selected a toroidal mixer, which is widely used commercially because of its ability to produce mRNA-LNPs with outstanding qualities [57,58]. To perform accurate and diverse evaluation of the mRNA-LNP formulations, we selected SARS-CoV-2 Spike mRNA for in vitro studies and FLuc mRNA for in vivo biodistribution assessments (Fig. 3A). The toroidal mixer has approximately 75-fold smaller internal volume per structure compared to the DVM. However, to perform a comprehensive and precise comparison, we produced three distinct formulations of DVM-LNPs and Toroidal-LNPs, keeping the process variables as consistent as

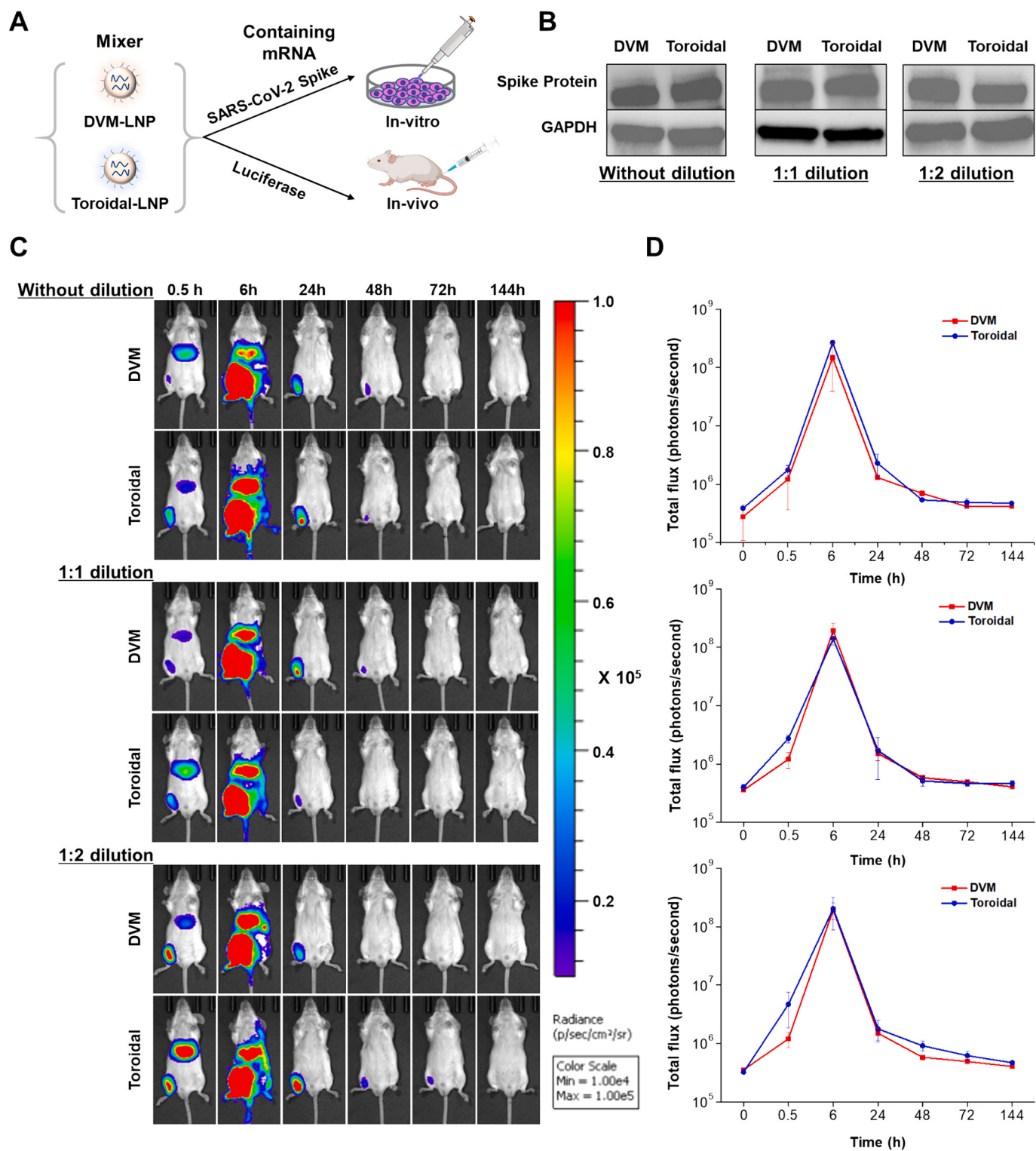


Fig. 3. Comparison of in vitro and in vivo protein expression of mRNA-LNPs generated using different mixers. (A) mRNA-LNPs with identical formulation conditions were either directly purified after production using DVM and a commercial toroidal mixer or subjected to in-line dilution at a flow rate ratio of 1:1 or 1:2 using PBS. mRNA-LNPs containing SARS-CoV-2 Spike mRNA were used for in vitro applications, whereas mRNA-LNPs containing FLuc mRNA were used for in vivo bio-distribution research. (B) Western blot results after cellular treatment of SARS-CoV-2 Spike mRNA-LNPs diluted to the same concentration. (Spike protein: 190 kDa, GAPDH: 37 kDa). (C) Bioluminescent imaging at specific time points after intramuscular (IM) injection of FLuc mRNA-LNP into male BALB/c mice. The image represents the 1st mouse within the $n = 3$ group. (D) Quantification of total luminescence values for each formulation in male BALB/c mice groups.

possible, including concentration, FRR, TFR, and the ratio of in-line PBS dilution. [59]. The properties of the purified LNP samples were compared for in vitro and in vivo protein expression (Table 1).

In all cases, uniform LNPs with a size of approximately 75–95 nm and a maximum PDI of 0.10 were produced. The EEs were also above 90%. Considering the volume difference between the DVM and the toroidal devices, the fact that both LNPs exhibited similar physicochemical properties under the same flow condition demonstrates the broad applicability of the DVM. Consecutively, the actual protein expression of both DVM-LNP and Toroidal-LNP were compared by treating to cells at the identical conditions and analyzed through Western blot, and showed similar protein expression in the cell lysate (Fig. 3B and Fig. S4).

For a comparative study of in vivo mRNA delivery for DVM-LNPs and Toroidal-LNPs, formulation conditions were maintained while altering only the mRNA component. For in vivo applications, no significant differences in the properties were observed between the DVM-LNPs and Toroidal-LNPs. After intramuscular (IM) injections, comparison of luminescence intensity over time showed comparable performance between groups with identical manufacturing processes, indicating uniform intensity. The highest level of luminescence similarity was observed in all the groups after 6 h. These luminescent phases persisted for 72 h and were completely gone after 144 h (Fig. 3C and D and Fig. S5). The results of bioluminescence over time showed equivalent biokinetic profiles and consistent mRNA delivery between DVM-LNPs and Toroidal-LNPs [60]. In essence, our findings confirm that despite its larger volume, the DVM platform exhibits precise processing capabilities through robust system control, resulting in mRNA-LNP properties similar to those of the commercially available toroidal mixer.

3.5. Long-term operation of the micromixer

In the drug delivery industry, consistent nanoparticle properties are critical for quality control in continuous manufacturing over long periods of time. The main factor affecting reactor performance is the aggregates that form inside the mixer during operation, which is the starting point for clogging [11–13]. To comparatively demonstrate the performance of DVM continuity, we constructed 3D-printed SVM, NVM, and DVM devices as two-piece assemblies (Fig. S6) in addition to a commercial reactor, transparent toroidal mixer [15]. And four types of micromixers were used to view the blockage during continuous nanoparticle manufacturing. In practice, continuous production of mRNA-LNPs for long period is inefficient and unrealistic with its high cost for quantifying/visualizing clogging within the channels. As an alternative, we chose to prepare fluorescent nanoparticles instead of mRNA-LNPs for efficient analysis. However, conventional dyes such as FITCs emit fluorescence in the molecular state in solution and are ineffective for long-term imaging and tracking, particularly when aggregated [61,62].

Table 1

Comparison of DVM and commercial toroidal mixers in the properties of purified mRNA-LNP under the same formulation conditions. The ratio given in the “In-line dilution” section represents the flow rate ratio of the total LNP solution to PBS (pH 7.4).

In vitro / In vivo	mRNA	Mixer	In-line dilution	Size (d, nm)	PDI	EE (%)
In vitro	SARS-CoV-2	DVM	–	92	0.10	92
			1:1	85	0.03	95
		Toroidal	1:2	76	0.09	93
	Firefly luciferase	DVM	–	95	0.09	94
			1:1	87	0.07	95
		Toroidal	1:2	81	0.10	95
In vivo	Firefly luciferase	DVM	–	83	0.07	96
			1:1	87	0.06	95
		Toroidal	1:2	88	0.05	96
	Toroidal	DVM	–	83	0.08	94
			1:1	82	0.07	95
		Toroidal	1:2	79	0.07	96

Therefore, we used tetraphenylethylene (TPE), an aggregation-induced-emission (AIE) molecule, for the clogging test. TPE allows us to observe only nanoparticles trapped inside the channel and overcomes the photoluminescence limitations associated with conventional FITCs [63–65]. The DVM precipitated highly uniform TPE nanoparticles with the smallest size of 77 nm when the FRR was increased to 9, followed by the toroidal mixer with 80 nm, the slow mixing SVM with 92 nm, and the NVM with 95 nm (Fig. 4A and Fig. S7). Because the wetting behavior of the colloidal solution with TPE nanoparticles and the material of the mixer may be different [66], the contact angles of the TPE nanoparticles on the toroidal reactor and the surface of the DVM were measured and confirmed the equivalent interaction (Fig. S8).

Based on the above experimental conditions, two High-performance liquid chromatography (HPLC) pumps with real-time pressure measurement capabilities were used to inject the solution and monitor the pressure changes inside the micromixers (Fig. S9). Continuous DLS analysis was also performed to check the variation in nanoparticle properties in real time. For 3D-printed mixers, TPE nanoparticles with constant physical characteristics were created over a period of approximately 1 h. However, the pressure difference in the SVM, NVM, and toroidal mixer increased to 454 psi and 266 psi, respectively, which dramatically changed the particle properties (Fig. 4B and C and Fig. S10). Owing to this high pressure, leakage occurred in the assembled SVM and NVM after 166 and 120 min of operation, respectively. In the case of the toroidal mixer, the same amount of clogging proved to be more fatal due to the small volume. Nanoparticles produced by the toroidal mixer exhibited a size of approximately 88 nm only after 30 min, which was around 10% larger than the initial size. After 100 min, the internal pressure of the toroidal mixer reached 254 psi. On the other hand, the pressure differential in the DVM was limited to 15 psi (460 min later), and the pressure inside the mixer was again maintained near the initial level for a total of 12 h despite continuous pump operation. Moreover, during continuous production of TPE nanoparticles for half a day, the PDI remained constantly below 0.1, whereas the size varied up to 5 nm.

After removing the leftover solution without affecting the clogged aggregates (until leakage from SVM and NVM, 100 min of toroidal mixer, 166 min, and 12 h of DVM each), the micromixers were disassembled for the further analysis. The degree of clogging in the micromixers was visualized using a microscope under UV irradiation (Fig. 4D and Fig. S11) [65]. A substantially larger luminescence intensity was observed in the case of the SVM, NVM, and toroidal mixer, especially where the obstruction inside the reactor led to an increase in pressure. In contrast, the DVM showed negligible clogging with an operating time of 166 min. Another DVM running for up to 12 h exhibited luminosity at the local outlet section; however, the internal channels responsible for vortex generation showed significantly lower luminosity than the other mixers. The remaining nanoparticle aggregates inside the mixers were once again dissolved using acetone, and their concentrations were quantified via UV-vis spectroscopy [67]. When converted to nanoparticle weight, SVM, NVM, and the toroidal mixer were 0.39 mg, 0.30 mg, and 0.10 mg, respectively. However, the DVM operated for 166 min amounted to only 0.03 mg, while the one operated for 12 h reached a mere 0.11 mg. Taking into consideration the total volume of the inner microstructures, the similarly operated DVM revealed >10 times less clogging compared to other types of baffles and remarkable 179-fold lower clogging ratio compared to the toroidal mixer (Fig. 4E and Fig. S12). This demonstrates that the relatively large reactor volume made by 3D-printing can lower the effect of aggregating nanoparticles in comparison to the toroidal mixer. In addition, based on the simulation results as aforementioned, the intensified vortex prevented the formation of aggregates by dispersing the nanoparticles *in situ*. Overall, DVM has demonstrated the capability to continuously produce various types of nanoparticles with high uniformity and desired sizes while minimizing property variations, serving as a foundational step towards scalability.

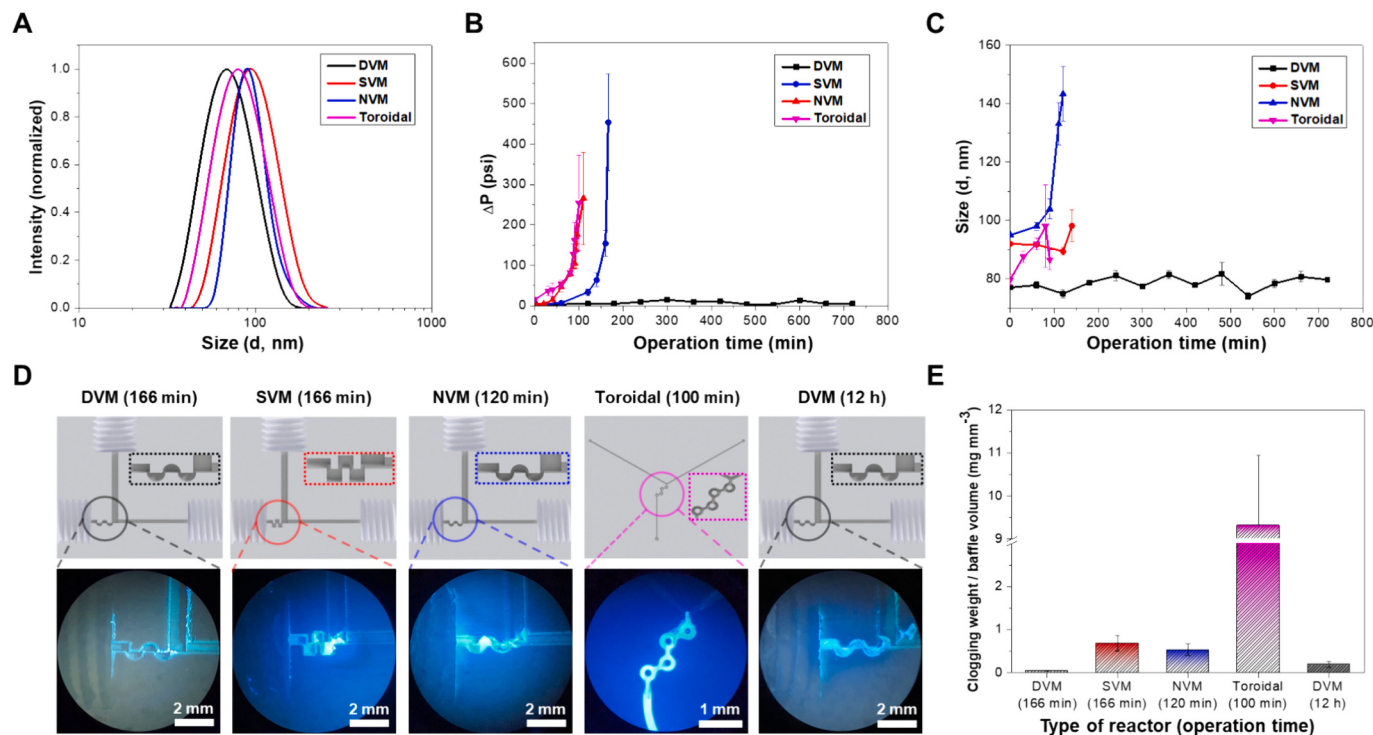


Fig. 4. Continuous production of TPE nanoparticles for validation of long-term use. (A) Normalized size distribution of initial TPE nanoparticles produced by various micromixers under identical flow rate conditions. (B) Real-time analysis of the pressure difference in the micromixers and (C) average size of the nanoparticles. (D) Fluorescence visualization of clogged TPE nanoparticles under the same ultraviolet irradiation intensity within disassembled mixers. (E) Quantified ratio between the weight of clogged aggregates and the volume of baffle.

4. Conclusion

In summary, we developed a novel micromixer with a three-dimensional structure, DVM, in response to the challenges faced by traditional microfluidic systems in therapeutic delivery, such as flow rate range, clogging, and difficulty in scaling up. The DVM intensify vortex, enabling rapid mixing and efficient nanoparticle dispersion at flow rates of just a few mL min^{-1} , thus mitigating the need for high flow rates and reducing the risk of clogging. The 3D-printed device allows for production of highly-uniform nanoparticles as a mRNA carrier across a wide range of concentrations, and shows comparable performance to commercially available ‘Nanoassembler Ignite’ platform in terms of protein expression and biokinetic profiles. Furthermore, the DVM demonstrates negligible pressure changes during continuous operation, even for 12 h, and its compact design facilitates potential for scalable production through one-step 3D-printing. This innovation holds great promise for enhancing nanoparticle production from laboratory research to large-scale clinical applications.

CRediT authorship contribution statement

Gi-Su Na: Writing – original draft, Visualization, Validation, Software, Methodology, Data curation, Conceptualization. **Jeong-Un Joo:** Visualization, Software. **Joo Young Lee:** Validation, Methodology, Formal analysis. **Yejin Yun:** Visualization, Validation, Formal analysis. **Byung Kwon Kaang:** Conceptualization. **Joo-Sung Yang:** Validation, Methodology, Conceptualization. **Kyungjin Kim:** Methodology, Investigation. **Dong-Pyo Kim:** Writing – review & editing, Validation, Supervision, Project administration, Funding acquisition.

Declaration of competing interest

The authors declare that they have no known competing financial interests or personal relationships that could have appeared to influence

the work reported in this paper.

Data availability

Data will be made available on request.

Acknowledgments

This work was supported by the National Research Foundation of Korea (NRF) grant funded by the Korea government (MSIP) (NRF-2017R1A3B1023598).

The authors would like to express their gratitude to Inyoung Lee and Jieun Lee, who assisted in the analysis of the experiments.

Appendix A. Supplementary data

Supplementary data to this article can be found online at <https://doi.org/10.1016/j.jconrel.2024.07.019>.

References

- [1] P.M. Cevala, A. Ali, E. Czuba-Wojnilowicz, J. Symons, S.R. Lewin, C. Cortez-Jugo, F. Caruso, ACS Nano 15 (2021) 3736–3753, <https://doi.org/10.1021/acsnano.0c09514>.
- [2] H. Maeda, H. Nakamura, J. Fang, Adv. Drug Deliv. Rev. 65 (2013) 71–79, <https://doi.org/10.1016/j.addr.2012.10.002>.
- [3] M.J. Mitchell, M.M. Billingsley, R.M. Haley, M.E. Wechsler, N.A. Peppas, R. Langer, Nat. Rev. Drug Discov. 20 (2021) 101–124, <https://doi.org/10.1038/s41573-020-0090-8>.
- [4] M. Danaei, M. Dehghankhord, S. Ataei, F. Hasanzadeh Davarani, R. Javanmard, A. Dokhani, S. Khorasani, M.R. Mozafari, Pharmaceutics 10 (2018) 57, <https://doi.org/10.3390/pharmaceutics10020057>.
- [5] X. Li, Z. Hu, J. Ma, X. Wang, Y. Zhang, W. Wang, Z. Yuan, Colloids Surf. B. Biointerfaces 167 (2018) 260–266, <https://doi.org/10.1016/j.colsurfb.2018.04.005>.
- [6] H. Cabral, Y. Matsumoto, K. Mizuno, Q. Chen, M. Murakami, M. Kimura, Y. Terada, M.R. Kano, K. Miyazono, M. Uesaka, N. Nishiyama, K. Kataoka, Nat. Nanotechnol. 6 (2011) 815–823, <https://doi.org/10.1038/nnano.2011.166>.

- [7] Y. Liu, G. Yang, Y. Hui, S. Ranaweera, C.X. Zhao, *Small* 18 (2022) 2106580, <https://doi.org/10.1002/smll.202106580>.
- [8] M.J.W. Evers, J.A. Kulkarni, R. Van Der Meel, P.R. Cullis, P. Vader, R. M. Schiffeler, *Small Methods* 2 (2018) 1700375, <https://doi.org/10.1002/smtd.201700375>.
- [9] A.D. Stroock, S.K.W. Dertinger, A. Ajdari, I. Mezić, H.A. Stone, G.M. Whitesides, *Science* 295 (2002) 647–651, <https://doi.org/10.1126/science.1066238>.
- [10] K.I. Min, D.J. Im, H.J. Lee, D.P. Kim, *Lab Chip* 14 (2014) 3987–3992, <https://doi.org/10.1039/c4lc00700j>.
- [11] E. Dressaire, A. Sauret, *Soft Matter* 13 (2017) 37–48, <https://doi.org/10.1039/C6SM01879C>.
- [12] K. Georgieva, D.J. Dijkstra, H. Fricke, N. Willenbacher, *J. Colloid Interface Sci.* 352 (2010) 265–277, <https://doi.org/10.1016/j.jcis.2010.08.065>.
- [13] K. Shahzad, W.V. Aeken, M. Mottaghi, V.K. Kamyab, S. Kuhn, *Microfluid. Nanofluid.* 22 (2018) 104, <https://doi.org/10.1007/s10404-018-2124-7>.
- [14] S.J. Shepherd, D. Issadore, M.J. Mitchell, *Biomaterials* 274 (2021) 120826, <https://doi.org/10.1016/j.biomaterials.2021.120826>.
- [15] C. Webb, N. Forbes, C.B. Roces, G. Anderluzzi, G. Lou, S. Abraham, L. Ingalls, K. Marshall, T.J. Leaver, J.A. Watts, J.W. Aylott, Y. Perrie, *Int. J. Pharm.* 582 (2020) 119266, <https://doi.org/10.1016/j.ijpharm.2020.119266>.
- [16] J.L. Santos, Y. Ren, J. Vandermark, M.M. Archang, J.M. Williford, H.W. Liu, J. Lee, T.H. Wang, H.Q. Mao, *Small* 12 (2016) 6214–6222, <https://doi.org/10.1002/smll.201601425>.
- [17] J. Feng, C.E. Markwalter, C. Tian, M. Armstrong, R.K. Prud'homme, *J. Transl. Med.* 17 (2019) 200, <https://doi.org/10.1186/s12967-019-1945-9>.
- [18] J.Y. Han, J.N. La Fiandra, D.L. DeVoe, *Nat. Commun.* 13 (2022) 6997, <https://doi.org/10.1038/s41467-022-34750-3>.
- [19] H. Kim, K.I. Min, K. Inoue, D.J. Im, D.P. Kim, J.I. Yoshida, *Science* 352 (2016) 691–694, <https://doi.org/10.1126/science.aaf1389>.
- [20] H.J. Lee, J.U. Joo, S.J. Yim, D.P. Kim, H. Kim, *Nat. Commun.* 14 (2023) 1231, <https://doi.org/10.1038/s41467-022-35611-9>.
- [21] N. Kimura, M. Maeki, Y. Sato, Y. Note, A. Ishida, H. Tani, H. Harashima, M. Tokeshi, *ACS Omega* 3 (2018) 5044–5051, <https://doi.org/10.1021/acsomega.8b00341>.
- [22] E. Kang, S.J. Shin, K.H. Lee, S.H. Lee, *Lab Chip* 10 (2010) 1856–1861, <https://doi.org/10.1039/c002695f>.
- [23] R. Tenchov, R. Bird, A.E. Curtze, Q. Zhou, *ACS Nano* 15 (2021) 16982–17015, <https://doi.org/10.1021/acsnano.1c04996>.
- [24] X. Hou, T. Zaks, R. Langer, Y. Dong, *Nat. Rev. Mater.* 6 (2021) 1078–1094, <https://doi.org/10.1038/s41578-021-00358-0>.
- [25] Q. Cheng, T. Wei, L. Farbiak, L.T. Johnson, S.A. Dilliard, D.J. Siegwart, *Nat. Nanotechnol.* 15 (2020) 313–320, <https://doi.org/10.1038/s41565-020-0669-6>.
- [26] F.P. Polack, S.J. Thomas, N. Kitchin, J. Absalon, A. Gurtman, S. Lockhart, J. L. Perez, G. Pérez Marc, E.D. Moreira, C. Zerbini, R. Bailey, K.A. Swanson, S. Roychoudhury, K. Kourty, P. Li, W.V. Kalina, D. Cooper, R.W. French, L. L. Hammitt, Ö. Türeci, N. Engl. *J. Med.* 383 (2020) 2603–2615, <https://doi.org/10.1056/nejmoa2034577>.
- [27] S.A. Dilliard, Q. Cheng, D.J. Siegwart, *Proc. Natl. Acad. Sci. U. S. A.* 118 (2021) e2109256118, <https://doi.org/10.1073/pnas.2109256118>.
- [28] M. Maeki, T. Saito, Y. Sato, T. Yasui, N. Kaji, A. Ishida, H. Tani, Y. Baba, H. Harashima, M. Tokeshi, *RSC Adv.* 5 (2015) 46181–46185, <https://doi.org/10.1039/c5ra04690d>.
- [29] A. Jahn, W.N. Vreeland, M. Gaitan, L.E. Locascio, *J. Am. Chem. Soc.* 126 (2004) 2674–2675, <https://doi.org/10.1021/ja0318030>.
- [30] S. Younoussi, A. Ettaouil, *Heliyon* 10 (2024) e24048, <https://doi.org/10.1016/j.heliyon.2024.e24048>.
- [31] T. Wei, H. Oprins, V. Cherman, E. Beyne, M. Baelmans 4 (2019) 145. doi: <https://doi.org/10.3390/fluids4030145>.
- [32] D. Dapelo, J. Bridgeman, *Water Sci. Technol.* 81 (2020) 1646–1657, <https://doi.org/10.2166/wst.2020.086>.
- [33] S. Dabiri, A. Noorpoor, M. Arfaee, P. Kumar, W. Rauch, *Water* 13 (2021) 1629, <https://doi.org/10.3390/w13121629>.
- [34] R. Othman, G.T. Vladisavljević, H.C. Hemaka Bandulasena, Z.K. Nagy, *Chem. Eng. J.* 280 (2015) 316–329, <https://doi.org/10.1016/j.cej.2015.05.083>.
- [35] I.V. Zhigaltshev, N. Belliveau, I. Hafez, A.K.K. Leung, J. Huff, C. Hansen, P.R. Cullis, *Langmuir* 28 (2012) 3633–3640, <https://doi.org/10.1021/la204833h>.
- [36] L. Schoenmaker, D. Witzigmann, J.A. Kulkarni, R. Verbeke, G. Kersten, W. Jiskoot, D.J.A. Crommelin, 601 (2021) 120586. doi: <https://doi.org/10.1016/j.ijpharm.2021.120586>.
- [37] R. Kumar, R. Chauhan, M. Sethi, A. Kumar, *Therm. Sci.* 22 (2016) 183–191, <https://doi.org/10.2298/TSCI151206125K>.
- [38] H.J. Lee, R.C. Roberts, D.J. Im, S.J. Yim, H. Kim, J.T. Kim, D.P. Kim, *Small* 15 (2019) 1905005, <https://doi.org/10.1002/smll.201905005>.
- [39] S. Shen, X. Wang, Y. Niu, *Micromachines* 12 (2021) 758, <https://doi.org/10.3390/mi12070758>.
- [40] G.J. Wang, K.H. Ho, S.H. Hsu, K.P. Wang, *Microdevices* 9 (2007) 657–663, <https://doi.org/10.1007/s10544-007-9067-1>.
- [41] G.M. Deloid, J.M. Cohen, G. Pyrgiotakis, P. Demokritou, *Nat. Protoc.* 12 (2017) 355–371, <https://doi.org/10.1038/nprot.2016.172>.
- [42] P. Jiang, W.S. Kim, T. Yu, A.C.S. Appl. Nano. Mater. 5 (2022) 9604–9614, <https://doi.org/10.1021/acsnano.2c01823>.
- [43] A.P. Sudarsan, V.M. Ugaz, *Proc. Natl. Acad. Sci. U. S. A.* 103 (2006) 7228–7233, <https://doi.org/10.1073/pnas.0507976103>.
- [44] J. Zhang, A.E. Tejada-Martínez, Q. Zhang, *Environ. Model. Softw.* 58 (2014) 71–85, <https://doi.org/10.1016/j.envsoft.2014.04.003>.
- [45] A. Jahn, S.M. Stavis, J.S. Hong, W.N. Vreeland, D.L. Devoe, M. Gaitan, *ACS Nano* 4 (2010) 2077–2087, <https://doi.org/10.1021/nn901676x>.
- [46] S. Yayla, S. Ayga, M. Oruç, *Renew. Energy* 157 (2020) 1243–1253, <https://doi.org/10.1016/j.renene.2020.05.027>.
- [47] M.S. Shah, J.B. Joshi, A.S. Kalsi, C.S.R. Prasad, D.S. Shukla, *Chem. Eng. Sci.* 71 (2012) 300–309, <https://doi.org/10.1016/j.ces.2011.11.022>.
- [48] E.K. Far, M. Geier, K. Kutschner, M. Krafczyk, *Computation* 5 (2017) 23, <https://doi.org/10.3390/computation5020023>.
- [49] J.M. Lim, A. Swami, L.M. Gilson, S. Chopra, S. Choi, J. Wu, R. Langer, R. Karnik, O. C. Farokhzad, *ACS Nano* 8 (2014) 6056–6065, <https://doi.org/10.1021/nn501371n>.
- [50] G.N. Ahn, M.J. Kim, S.J. Yim, B.M. Sharma, D.P. Kim, *ACS Sustainable Chem. Eng.* 10 (2022) 3951–3959, <https://doi.org/10.1021/acssuschemeng.1c08240>.
- [51] J. Safka, M. Ackermann, D. Martis, MM Sci. J. (2016) 1573–1578, <https://doi.org/10.17973/MMSJ.2016.12.2016185>.
- [52] H.S. Choi, G. Ahn, G. Na, H.J. Cha, D.P. Kim, A.C.S. Biomater., Sci. Eng. 8 (2022) 4577–4585, <https://doi.org/10.1021/acsbiomaterials.2c00435>.
- [53] F. Zhao, D. Cambié, J. Janse, E.W. Wieland, K.P.L. Kuijpers, V. Hessel, M.G. Debije, T. Noël, ACS Sustain. Chem. Eng. 6 (2018) 422–429, <https://doi.org/10.1021/acssuschemeng.7b02687>.
- [54] M.M. Allyn, R.H. Luo, E.B. Hellwarth, K.E. Swindle-Reilly, *Front. Med.* 8 (2022) 787644, <https://doi.org/10.3389/fmed.2021.787644>.
- [55] J. Hrkach, D. Von Hoff, M.M. Ali, E. Andrianova, J. Auer, T. Campbell, D. De Witt, M. Figa, M. Figueiredo, A. Horhota, S. Low, K. McDonnell, E. Peeke, B. Retnarajan, A. Sabnis, E. Schnipper, J.J. Song, Y.H. Song, J. Summa, D. Tompsett, et al., *Sci. Transl. Med.* 4 (2012) 128ra39, <https://doi.org/10.1126/scitranslmed.3003651>.
- [56] W. Deng, W. Chen, S. Clement, A. Guller, Z. Zhao, A. Engel, E.M. Goldys, *Nat. Commun.* 9 (2018) 2713, <https://doi.org/10.1038/s41467-018-05118-3>.
- [57] S. Meulewaeter, G. Nuyttten, M.H.Y. Cheng, S.C. De Smedt, P.R. Cullis, T. De Beer, I. Lentacker, R. Verbeke, *J. Control. Release* 357 (2023) 149–160, <https://doi.org/10.1016/j.jconrel.2023.03.039>.
- [58] A.K. Blakney, P.F. McKay, K. Hu, K. Samuan, N. Jain, A. Brown, A. Thomas, P. Rogers, K. Polra, H. Sallah, J. Yeow, Y. Zhu, M.M. Stevens, A. Geall, R. J. Shattock, *J. Control. Release* 338 (2021) 201–210, <https://doi.org/10.1016/j.jconrel.2021.08.029>.
- [59] N. Kimura, M. Maeki, Y. Sato, A. Ishida, H. Tani, H. Harashima, M. Tokeshi, *ACS Appl. Mater. Interfaces* 12 (2020) 34011–34020, <https://doi.org/10.1021/acsmi.0c05489>.
- [60] L.I. Zheng, S.R. Bandara, Z.I. Tan, C. Leal, *Proc. Natl. Acad. Sci. U. S. A.* 120 (2023) e2301067120, <https://doi.org/10.1073/pnas.2301067120>.
- [61] R.T.K. Kwok, C.W.T. Leung, J.W.Y. Lam, B.Z. Tang, *Chem. Soc. Rev.* 44 (2015) 4228–4238, <https://doi.org/10.1039/c4cs00325j>.
- [62] D. Ding, K. Li, B. Liu, B.Z. Tang, *Acc. Chem. Res.* 46 (2013) 2441–2453, <https://doi.org/10.1021/ar3003464>.
- [63] B. Wang, S. Liu, X. Liu, R. Hu, A. Qin, B.Z. Tang, *Adv. Healthc. Mater.* 10 (2021) 2101067, <https://doi.org/10.1002/adhm.202101067>.
- [64] M.P. Aldred, C. Li, M.Q. Zhu, *Chem. A Eur. J.* 18 (2012) 16037–16045, <https://doi.org/10.1002/chem.201202715>.
- [65] W. Li, J. Chen, S. Zhao, T. Huang, H. Ying, C. Trujillo, G. Molinaro, Z. Zhou, T. Jiang, W. Liu, L. Li, Y. Bai, P. Quan, Y. Ding, J. Hirvonen, G. Yin, H.A. Santos, J. Fan, *Nat. Commun.* 13 (2022) 1262, <https://doi.org/10.1038/s41467-022-28787-7>.
- [66] A. Maestro, E. Guzmán, F. Ortega, R.G. Rubio, *Colloid Interface Sci.* 19 (2014) 355–367, <https://doi.org/10.1016/j.cocis.2014.04.008>.
- [67] M.J. Robb, W. Li, R.C.R. Gergely, C.C. Matthews, S.R. White, N.R. Sottos, J.S. A. Moore, *ACS Cent. Sci.* 2 (2016) 598–603, <https://doi.org/10.1021/acscentsci.6b00198>.